Coalescence of concentrated emulsions in microfluidic constrictions through avalanches

Hinderink, Emma; Bera, Bijoy; Schinkel, Christiaan; Steijn, Volkert van

DOI
10.1038/s41598-025-87291-2

Publication date
2025

Document Version
Final published version

Published in
Scientific Reports

Citation (APA)
Hinderink, E., Bera, B., Schinkel, C., & Steijn, V. V. (2025). Coalescence of concentrated emulsions in microfluidic constrictions through avalanches. *Scientific Reports*, *15*(1), Article 5720. https://doi.org/10.1038/s41598-025-87291-2

scientific reports

OPEN

Coalescence of concentrated emulsions in microfluidic constrictions through avalanches

Emma Hinderink[1,2]✉, Bijoy Bera[1], Christiaan Schinkel[1] & Volkert van Steijn[1]

Concentrated emulsions flowing through channels of varying widths are omnipresent in daily life, from dispensing mayonnaise in our kitchens to large-scale industrial processing of food, pharmaceuticals, etc. Local changes in channel geometry affect the stability of emulsions over length scales far beyond the droplet magnitude, for example through propagation of coalescence events called a coalescence avalanche. The underlying mechanisms are not well understood. In this work, we investigated the stability of concentrated emulsions flowing through microchannels featuring a constriction. We found that in this model geometry, the acceleration of the droplets induced near the entrance of the constriction triggers a coalescence event between the leading and the trailing droplet, but only above a critical droplet velocity. This separation-induced coalescence event, in turn, was found to trigger a coalescence avalanche in the upstream direction. Analysis of the flow behavior through particle image velocimetry and particle tracking velocimetry revealed that the propagation also follows a separation-induced coalescence mechanism, due to the retraction of the interface of the trailing droplet upon coalescence and the corresponding acceleration of the liquid inside the coalesced fluid thread. The constriction ratio was found to enhance the coalescence occurrence but did not affect the speed of coalescence propagation.

Keywords Coalescence avalanche, Coalescence propagation, Particle image velocimetry

Emulsions are ubiquitous in industrial processes, and they are usually subjected to flows during such processing, for example, while being transported through nozzles, pipes, or membranes[1]. The flow might induce emulsion destabilization, such as droplet break-up or coalescence. In such cases, interactions between two or more droplets play an important role. Especially in concentrated emulsions (i.e., emulsions with a dispersed volume fraction higher than random close packing), droplet-droplet contact and interactions affect the emulsion properties[2]. In many cases, minimizing flow-induced changes is crucial for maintaining the quality of emulsion-based products. In some cases, controlled coalescence is desired, for example during phase-inversion and separation processes. Therefore, understanding coalescence in flowing concentrated emulsions is of importance.

Coalescence, and more specifically, drainage of the thin film between two droplets, has been studied extensively. Important model systems include measurements of the thin film drainage between a droplet and a flat surface or between two isolated droplets[3–6]. To get insights into the coalescence dynamics of emulsions under flow, microfluidic devices are particularly useful. They allow precise control over droplet velocity, droplet diameter, droplet packing, collision angle, temperature and, geometry[7–11]. In addition, coalescence can be studied at the length scale of individual droplets, which is not possible in bulk emulsions due to their turbidity. For example, a rather counter-intuitive phenomenon was observed in a microchannel of varying width (i.e., containing expanding and contracting cross-sections), which induced deceleration and acceleration of two co-flowing droplets. Instead of coalescing when pressed together during deceleration of the leading droplet, coalescence occurred while the leading droplet accelerated away from the trailing droplet[12–14]. This separation-driven coalescence mechanism is attributed to the reduction in hydrodynamic pressure inside the thin film between the droplets, which induces film thinning[15]. Furthermore, the reduced pressure in the thin film induces local deformations at the droplet interfaces[14]. When these deformed droplet interfaces are not rapidly stabilized through redistribution and adsorption of surfactants, the droplets coalesce[12,14]. Although these studies were conducted for two droplets, insights can be translated to more complex emulsion systems with higher droplet volume fractions as was shown by Bremond *et al.*[16].

[1]Department of Chemical Engineering, Delft University of Technology, 2629 HZ Delft, The Netherlands. [2]Multiphase Systems (ME-P&E), Delft University of Technology, 2628 CN Delft, The Netherlands. ✉email: e.hinderink@tudelft.nl

An intriguing phenomenon in flowing concentrated emulsions is that one coalescence event may trigger another coalescence event, leading to a gradual propagation of such events, known as a coalescence avalanche. Some researchers argued that the leading coalesced droplet moves at a lower velocity due to the increased drag allowing the trailing droplet to catch-up and cause a new coalescence event[17]. On the other hand, many others attributed the coalescence propagation to interface relaxation of the just-coalesced droplet and its subsequent separation (i.e., acceleration of leading droplet) from the trailing droplet[13,16]. This then leads to separation-induced coalescence. The pioneering work of Bremond *et al.*[16] has been widely utilized to explain the physical origin of coalescence avalanches in other experimental studies[17–19]. Furthermore, it has served as a basis for Monte Carlo simulations to study the effect of droplet packing on coalescence propagation. The propagation was more extensive in hexagonal closed-packed droplet assemblies compared to random closed-packed ones[20,21]. The probability of initiating a new coalescence event was found to depend on the angle between the leading and the trailing droplets. The probability was highest at 0°, while no coalescence events occurred above 130°[16,20].

The dynamics of the thin film drainage along with interface retractions are expected to be the basis of the start of coalescence around the constriction and its subsequent propagation. This conjecture and the underlying fluid dynamics have never been systematically investigated using experimental techniques. In this work, we investigate the effect of acceleration on the onset of coalescence and subsequent propagation into avalanches. To this end, we developed microfluidic coalescence devices containing various geometrical constrictions to systematically control the acceleration pathways. We quantify the coalescence frequency as a function of droplet velocity for the various geometries. Finally, we scrutinize the flow dynamics in the coalescence avalanches in concentrated water-in-oil (w/o) emulsions using a state-of-the-art particle image velocimetry (PIV) set-up to conduct micro-PIV and particle tracking velocimetry (PTV). The flow dynamics within the avalanche provide valuable insights into the physical mechanisms that induce coalescence far away, and even in absence, of constrictions.

Results and discussion

Stability of concentrated emulsions

In the reference chip, the droplets did not coalesce within the experimental range of flow rates. More specifically, the mono-disperse emulsion flowed stably through the channel, with three to four droplets spanning over the width of the channel (Fig. 1A). By contrast, coalescence was observed in the channels with constriction. Notably, coalescence was not observed in all frames. We observed intermittent coalescence behavior, as evident from the snapshots that show both non-coalesced droplets (Fig. 1A, 45°, left) and coalesced droplets (Fig. 1A, 45° right) over time. Fig. 1B shows the corresponding relative frequency of the droplet volumes before and after the constriction. It is clear that after the constriction, the droplet volumes increased due to coalescence. However, many of the droplets did not coalesce ($f_{coal} \sim 0.5$), i.e., each droplet coalesced on average 0.5 times.

To quantify the effect of the flow velocity and the constriction geometry on emulsion stability, we measured the coalescence frequency. In the set of three devices with different constriction angles (45, 60, and 90°) and a fixed constriction ratio of 2:1, virtually no coalescence was observed for droplet velocities below ~0.005 m/s, translating in a near zero coalescence frequency (Fig. 1C). Above this velocity, the coalescence frequency

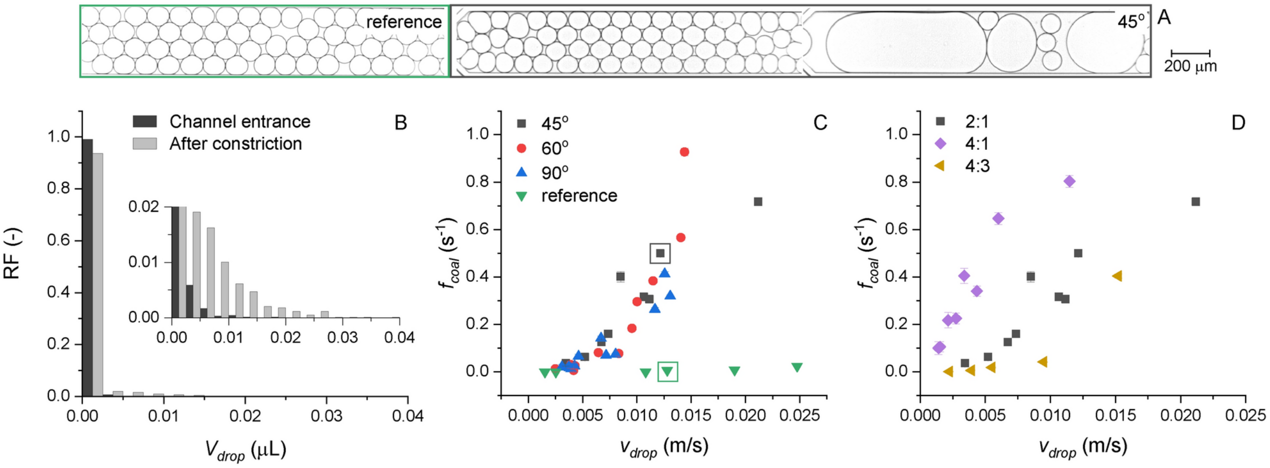

Fig. 1. (**A**) Representative snapshots of the concentrated emulsion flowing through the reference chip at 1.5 cm from the entrance and two representative snapshots in a constriction chip (45°, 2:1) at the downstream side of the constriction, illustrating the temporal nature of coalescence behavior. (**B**) Relative frequency (RF) of the droplet volumes (V_{drop}) present before and after the constriction in the constriction chip (45°, 2:1). Insert shows a zoom of the plot to show the larger droplets present at lower frequencies. (**C**) Coalescence frequency (f_{coal}), measured at the downstream side of the constriction, for the studied range of flow rates, in constriction chips with different constriction angles (45, 60, and 90°) and a fixed constriction ratio (2:1). Snapshots of the emulsions for the data points highlighted by the boxes are shown in (**A**). The distribution of droplet volumes corresponding to the data point in the black box is shown in (**B**). (**D**) Coalescence frequency in chips with different constriction ratios (4:1, 2:1, and 4:3) and a fixed length of 10 μm over which the channel constricts.

increased as droplet velocity increased, independent of the constriction angle. By contrast, the width of the constriction has a pronounced effect on the coalescence frequency (Fig. 1D). In the widest constriction (ratio of 4:3), coalescence was induced at droplet velocities above 0.01 m/s, while this onset velocity was more than five times lower in the narrowest constriction (ratio of 4:1, coalescence at droplet velocity of 0.015). These results are in line with simulations showing that separation-induced coalescence is favored by higher separation velocities[15]. This was explained by the higher hydrodynamic attractive forces upon faster separation[6]. Calculating the acceleration ($\delta v/\delta t$) of the droplets shows that the onset of coalescence occurred at ~0.4 $\mathrm{m/s^2}$ for all chips, except the 4:1 chip. For the latter, coalescence was already initiated at acceleration speeds of ~0.2 $\mathrm{m/s^2}$.

Due to the acceleration of the leading droplet the pressure in the film between the two droplets decreases. As the droplets move further apart, the pressure continues to drop, leading to interfacial deformation[22,23]. The temporary increase in interfacial area dilutes the concentration of adsorbed surfactants[24]. If not readily stabilized via Marangoni flows or adsorption of new surfactants from the continuous phase, the deformed interface is more prone to coalescence. The competition between the time scale at which the droplets deform and at which their interface stabilizes may explain the onset acceleration i.e., at lower acceleration droplet deformation is lower and there is more time for surfactant re-adsorption. In the chip with a constriction width of 4:1, a lower onset acceleration was measured. In this geometry, the droplet size is larger than the constriction width. When flowing through the constriction the droplets are extensively deformed by the channel walls (Figs. 6, 7), reducing the surface coverage and making the droplets more prone to coalescence. Furthermore, droplets obtain a small radius of curvature when flowing through the constriction, which reduces the thin film volume and may thus favor coalescence[16].

Deformation near the constriction occurs in the millisecond range, highlighting the importance of studies on dynamic interfacial tension and surface coverage at these short timescales[24,25]. The exact composition and molecular weight of the commercially available surfactant Pico-surf used is unknown but is expected to be around 12,600 g/mol (containing two perfluoropolyether (PFPE) blocks linked to a polyethylene glycol (PEG)[11].) As diffusion time-scale increases with increasing molecular weight of the surfactant, it is highly unlikely that Pico-surf can adsorb from the bulk to the interface during the relevant time-scales of deformation. To exemplify, the low molecular weight surfactant sodium dodecyl sulfate (388 g/mol) has a diffusion time-scale of around 0.9 ms[26]. That of Pico-surf is expected to be orders of magnitude larger and hence beyond the observed time scale of interface deformation.

Besides coalescence, droplet break-up is a phenomenon occurring when concentrated emulsions flow through constrictions[27–30]. We did not observe any break-up of non-coalesced droplets in our experiments. This can be explained by the relatively low values of the capillary number at which the experiments were performed (upper limit is 10^{-2}). The break-up is expected to occur at larger values as, for example, reported by Rosenfeld *et al.*[29] for highly deformed concentrated droplets entering a microfluidic constriction.

Avalanches as primary coalescence mechanism

Coalescence of the concentrated emulsion droplets is induced near the entrance of the constriction, as illustrated in the three snapshots in Fig. 2A. The primary mechanism responsible for the further destabilization of the flowing concentrated emulsions is the upstream propagation of coalescence events, see Fig. 2B and movie S1 in Supplementary Information. These coalescence avalanches have been reported in the past for concentrated confined water-in-oil emulsions[13,16,18]. They are explained as follows: once coalescence is induced, by acceleration of the flow in a constriction, the interface of the coalesced droplet retracts. This retraction pulls the interface away from the trailing droplet, leading to a reduction of the pressure in the film between the droplets. As a result, the film drains and eventually ruptures[12,13,16]. This is indeed visible in our experiments, as illustrated for one coalescence propagation event in greater detail in Fig. 2C. Just after coalescence, the spherical shape of the most recently coalesced droplet is clearly visible ($t = 0$ ms). This interface relaxes, evening out curvature differences through the internal flow from the spherical back to the upstream neck. As a result of the induced thinning of the film, the interfaces of the leading and trailing droplets deform and become pointy prior to coalescence, as clearly visible in the snapshot at $t = 3$ ms. The coalesced droplet, having a spherical trailing part, connected to a thinner neck upstream, as shown at $t = 4$ ms, again relaxes, culminating in an avalanche. We note that coalescence propagation occurred over large distances in the upstream direction, at times even from the constriction completely up to the entrance of the coalescence channel. While the illustrations in Fig. 2 may suggest that the propagation occurs between droplets in the same row of the packing, propagation was sometimes also observed between droplets in different rows. As discussed by Bremond and co-workers, the coalescence probability is highest in the direction of the downstream flow and decreases with increasing angle between the coalesced and trailing droplet[16]. Thus, coalescence between droplets in different rows may occur.

Flow dynamics from PIV and PTV

So far, we have shown that the velocity difference between the leading and trailing droplets was the basis for the initial coalescence event near the entrance of the constriction. The phenomenon of coalescence induced by acceleration from constriction is well-documented in the literature, as outlined in previous sections[6,15,22,23]. However, while several authors have described upstream propagation based on observations from brightfield images[16,18], no experimental data is present about the underlying fluid flow. Therefore, to gain more insights into the relaxation of just-coalesced droplets during an avalanche, we visualized the dispersed phase flow using PIV and PTV. These techniques have been proven to be instrumental in furthering our understanding of the coalescence of isolated droplets[31–36]. For example, PIV measurements of two co-flowing droplets revealed that the velocity field in the leading droplet was not affected by their coalescence, while the liquid in the trailing droplet accelerated until the coalesced droplet pair reached its equilibrium shape[32]. More recently, the flow fields inside droplets of a concentrated non-coalescing emulsion, flowing through a straight or tapered microchannel,

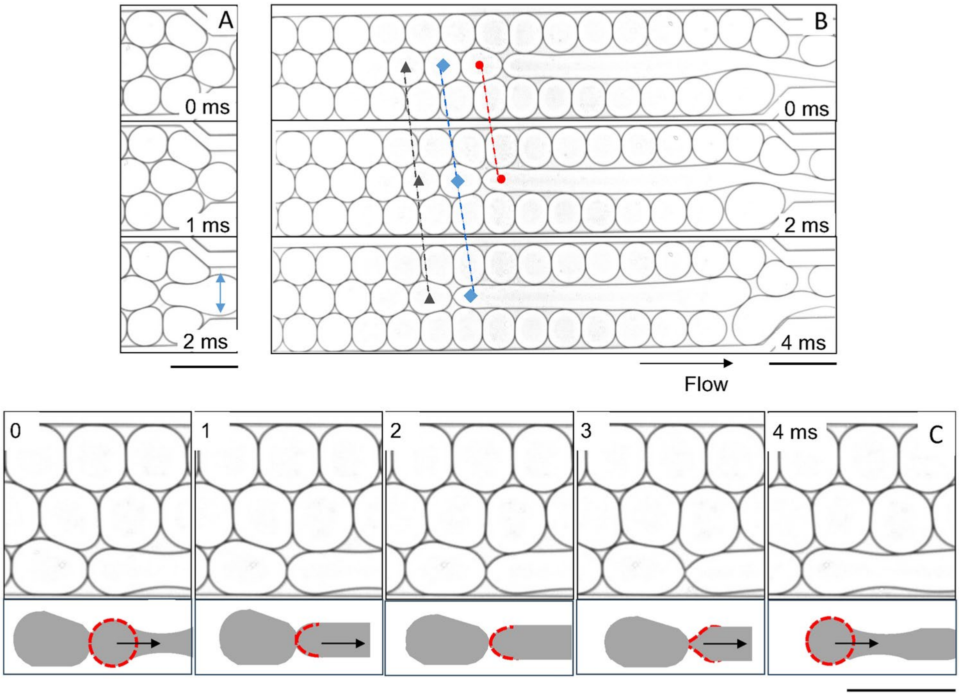

Fig. 2. (**A**) Coalescence induced by the constriction is evident from the three snapshots recorded at a temporal resolution of 1 ms. (**B**) Illustration of a coalescence avalanche in which coalescence of droplets, induced at the entrance of the constriction, propagates upstream. (**C**) Illustration of the propagation mechanism, with the relaxation of the interface of the just-coalesced droplet leading to a separation from the trailing droplet, resulting in drainage and rupture of the thin film between them. All brightfield images were recorded in the constriction chip with 45° angle and 2:1 constriction ratio.

have been studied[37,38]. In these emulsions, the fluid inside the droplets flows in a rotational manner i.e., internal circulation. This flow inside the droplets is induced by the flow of the continuous phase as well as shear forces arising from droplet confinement[37]. The rotational structures are dependent on the droplet packing and vary from single droplets or dilute emulsions since the fluid motion is affected by the shear forces of flowing neighboring droplets[38].

Until now, the fluid flow during coalescence avalanches has never been visualized or quantified. We expect that insights into the flow within the coalescence avalanches, will help us further understand the mechanism of upstream coalescence propagation, as will be further discussed in the next sections.

Particle image velocimetry

The PIV analysis is focused on the flow field at three specific instances of the intermittent coalescence behavior: 1) no coalescence, 2) coalescence with an avalanche propagating over about half of the field of view, and 3) coalescence with an avalanche propagating over the full field of view. Without coalescence, the emulsion flows like a plug through the channel with an almost uniform velocity across the channel width (panels 1, Fig. 3). The velocities increase near the entrance of the constriction and are about two times higher in the constriction than in the main channel for the 2:1 constriction, and 4 times for the 4:1 constriction. Analysis of the velocity fields during coalescence propagation reveals a clear increase in velocity within the propagating aqueous threads (panels 2 and 3, Fig. 3). In both the main channel and the constriction, the velocities within the coalescence avalanche are higher than the ones present before coalescence. This supports the hypothesis that the coalesced droplet accelerates and retracts from the trailing droplet, as described before and illustrated in Fig. 2C.

To elucidate if the acceleration of the fluid in the coalescence avalanche is a result of the acceleration of the fluid thread in the constriction, we compare the velocity fields of non-coalesced and coalesced emulsions in both chips. While the velocity of the non-coalesced emulsion in the constriction is twice as large in the 4:1 constriction as compared to the 2:1 constriction (panels 1, Fig. 3), the velocity in the coalesced thread is about the same in the main channels (panels 2 and 3, Fig. 3). This is more clearly seen in Fig. 4, which features the velocity profiles across the main channel. While the velocity profile of the incoming non-coalesced emulsions (open symbols) is flat and about the same (0.005 ± 0.001 m/s and 0.006 ± 0.001 m/s for the 2:1 and 4:1 constriction ratios, respectively), the velocity profiles in the propagating thread almost overlap. The independence of this velocity in the thread on the velocity in the constriction can be understood from the fact that the liquids are driven into the channel at a constant flow rate. Mass conservation hence leaves no room for the coalesced thread to be pulled through the constriction at the local velocity in the constriction. We hence conclude that the increasing coalescence frequency (0.06 for 2:1 at 0.05 m/s and 0.35 for 4:1 at 0.04 m/s, see Fig. 1C) arises from the chance that an avalanche occurs, not from the flow features of the avalanche itself.

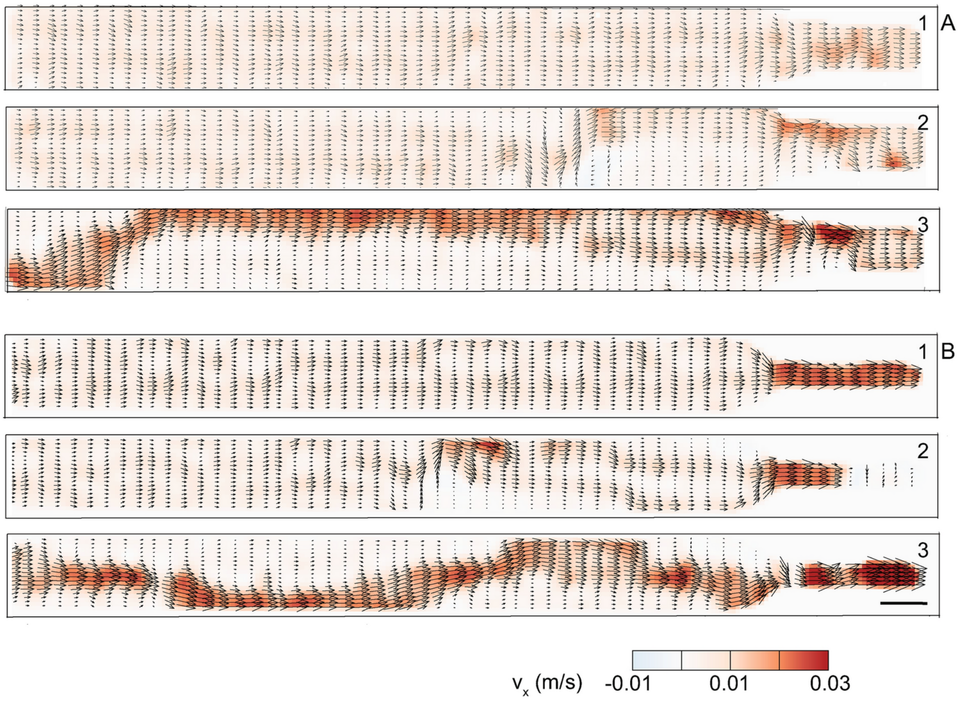

Fig. 3. Velocity fields obtained from PIV in the mid-plane of the coalescence channels with a constriction ratio of (**A**) 2:1 (45°) and (**B**) 4:1 (57°). From top to bottom: (1) no coalescence, (2) propagation of a coalescence avalanche over half of the field of view, and (3) over the entire field of view. The dispersed phase is seeded with tracer particles and visualized. Scale bar: 200 µm.

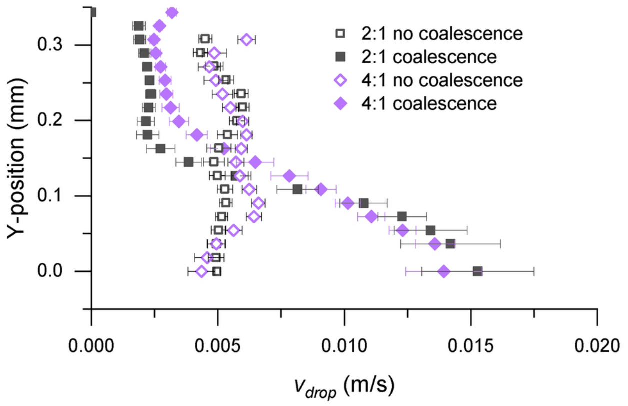

Fig. 4. Velocity profiles across the width of the coalescence channel in the channels with 2:1 (45°) and 4:1 constriction ratios, without (open symbols) and with (closed symbols) the propagation of a coalescence avalanche. The *y*-positions are presented such that the location of the avalanche is on the same side. Error bars represent the standard deviation around the mean velocity at a given *y*-position for at least 10 consecutive velocity fields.

Finally, we highlight an interesting feature of the flow visible near the location of the most recent coalescence event. As shown by the light blue regions, the local flow is in the direction opposite of the main flow (panels 2, Fig. 3). During coalescence, the thin film empties which may lead to counter-rotation of the droplets next to the area where the thin film breaks[39,40]. Furthermore, the high velocity of the coalescence avalanche next to the slower-moving non-coalesced droplets gives rise to a shear flow which further enhances the formation of the counter-rotating structures[35].

Particle tracking velocimetry

To obtain a higher level of detail, we also analyzed the images using a particle tracking velocimetry (PTV) algorithm. To this end, individual seeding particles were tracked over time using the Shake-The-Box algorithm[41].

Without coalescence, the emulsion flows in a three-row assembly through the main channel as discussed before. Traces of this assembly are visible by the particle tracks in panels 1 of Fig. 5, where the curved trajectories are reminiscent of the flow near the interfaces of the droplets, which is faster than the flow in the center of the droplets as well-known for (assemblies of) droplets flowing through confining geometries[38].

During coalescence propagation, the velocity near the interface of the coalesced thread is higher than in the core of the thread (panels 2 and 3, Fig. 5). The velocity near the interface of the coalesced thread increased up to 0.03 m/s, which is higher than present in the non-coalesced system (panels 1). After complete propagation, parts of the core of the thread are also at higher velocities than before (panels 3, Fig. 5). While the coalesced fluid thread has an almost constant width across the field of view in the bottom panel of Fig. 5A, significant variations in width, and hence significant variations in velocity, are seen in the coalesced thread in the bottom panel of Fig. 5B.

These new details illustrate the added value of the additional PTV analysis since these were not observed in the corresponding PIV analysis (panels 2 and 3, Fig. 3). This is better seen in the time-resolved movies S2 and S3 in Supplementary Information. However, we also note the shortcomings of the PTV analysis. The Shake-The-Box algorithm predicts the particle's next position by extrapolation the particle trajectories from previous time steps. During coalescence, the flow dynamics cannot be resolved by the algorithm, as evident from the missing trajectories at the downstream side of the fluid thread during propagation (panels 2 in Fig. 5, and movie S2 and S3 in Supplementary Information).

Taking the brightfield, PIV, and PTV results together, we can thus confirm that 1) dispersed phase flow acceleration is the physical phenomenon triggering the coalescence propagation and 2) that the acceleration is most pronounced at the interfacial region of the coalesced thread. This work highlights the importance of analyzing the flow at a much larger length scale than that of a single droplet.

Conclusion

In this work, we studied the stability of concentrated water-in-oil (w/o) emulsions flowing through a microfluidic channel featuring a constriction with varying geometries. We used PIV and PTV to obtain insights into the underlying dispersed phase flow. The surfactant concentration was chosen such that virtually no coalescence was observed in a reference chip without constriction, while significant coalescence was observed in the microchannels with constrictions. Above a critical onset velocity, coalescence was induced near the entrance of the constriction where a leading droplet accelerates away from a trailing droplet. This separation-induced coalescence mechanism explains why the constriction width was found to influence the onset velocity and the coalescence frequency, while the constriction angle was found to play no role. After an initial coalescence event, coalescence propagates upstream. These coalescence avalanches, at times even extending from constriction to entrance, are the main contributors to the change in the droplet size distribution of the concentrated emulsion. Subsequent analysis of the propagation of the avalanches through PIV and PTV revealed that propagation of coalescence also occurs through a separation-induced mechanism: relaxation of the interface of the just-

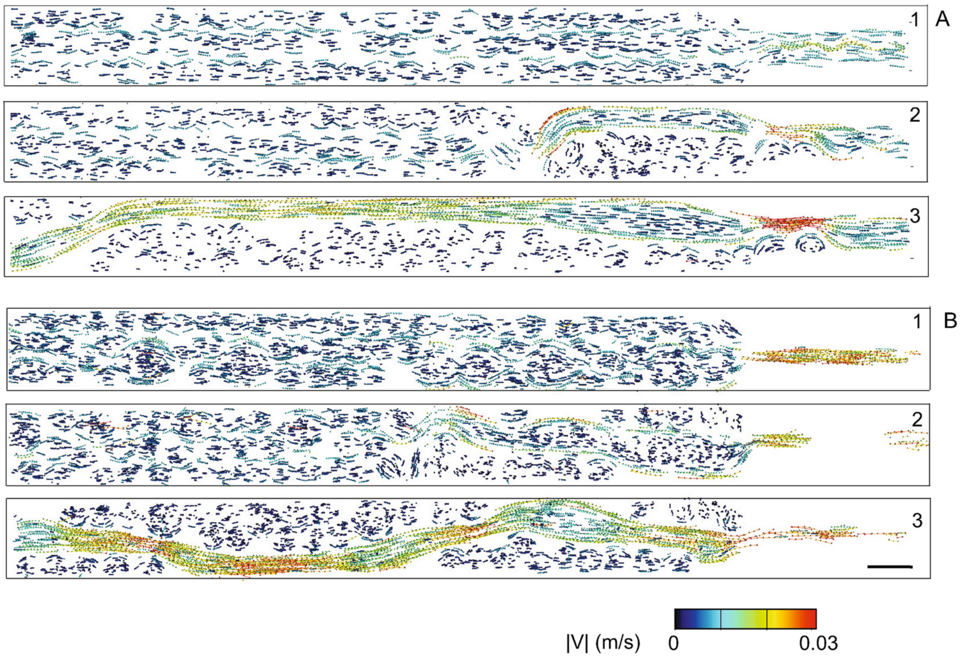

Fig. 5. Particle trajectories and absolute velocities (V) from PTV corresponding to the PIV results presented in Fig. 3. From top to bottom: (1) no coalescence, (2) propagation of a coalescence avalanche over half of the field of view, and (3) over the entire field of view. The dispersed phase is seeded with tracer particles and visualized. Scale bar: 200 µm.

coalesced droplet away from the trailing droplet causes the flow inside the coalesced thread to be faster (0.01-0.015 m/s) than that of the non-coalesced droplets ($\sim$0.005 m/s), leading to a subsequent coalescence event upstream. While the constriction and its width are instrumental in triggering the initial coalescence event, the velocity inside the coalesced thread was found to be independent of the local velocity in the constriction. Our findings highlight the complex fluid dynamics triggering these events.

Finally, our study elucidates the impact of locally induced coalescence on the destabilization of concentrated w/o emulsions flowing through non-straight microchannels through coalescence avalanches. Several studies report coalescence avalanches in w/o emulsion flowing through microchannels[12,13,16–19]. A natural extension to this work is to study the stability of concentrated oil-in-water (o/w) emulsions in microchannels, for which coalescence avalanches have not been reported in the literature. Further insights on the (dis)similarities between o/w and w/o emulsions may for example contribute to a thorough understanding of shear-induced phase inversion during processing of concentrated emulsions.

Methods

Microfluidic device design

The design of the microfluidic devices comprises three main features: a T-junction, a filter, and a coalescence channel with constriction (Fig. 6[42]). The height of the channels is uniform in all devices and equal to 55 μm. Droplets are continuously formed in the dripping/squeezing regime at the T-junction, comprising 100 μm wide channels. The droplets enter the 800 μm wide main channel in which they relax to a circular shape (as seen in the two-dimensional top-view images). Droplets pack to a concentrated emulsion near the entrance of the coalescence channel through the extraction of the continuous phase via the filter and the 175 μm wide bypass channels aside from the coalescence channel. A constriction is located 1 cm downstream of the entrance of the 350 μm wide and 2 cm long coalescence channel. The influence of the geometry of the constriction on the stability of the flowing concentrated emulsions was studied for constrictions with different constriction angles and constriction widths. The effect of the constriction angle (45, 60, and 90°) was studied in 175 μm wide constrictions corresponding to a constriction ratio of 2:1. The effect of the constriction width (87.5, 175, and 262.5 μm), corresponding to constriction ratios of 4:1, 2:1, and 4:3 was studied in devices with a fixed length of 10 μm over which the main channel constricts, resulting in constriction angles of 57, 45, and 26°, respectively. Reference measurements were performed in a device without a constriction in the coalescence channel.

Microfluidic device fabrication

We fabricated our microfluidic devices using soft lithography, with the lithographic steps performed in a clean room. In short, a 4-inch silicon wafer was spin-coated at 3000 rpm for 30 seconds with a negative photoresist (SU8-3500, Micro Resist Technology GmbH, Germany) and soft-baked at 100°C for 15 minutes. The height of the photoresist layer was 55 μm as determined by a profilometer (DektakXT 2, Bruker, Billerica, US). The two-dimensional designs were made in AutoCAD (Autodesk) and printed on the coated wafer with a tabletop

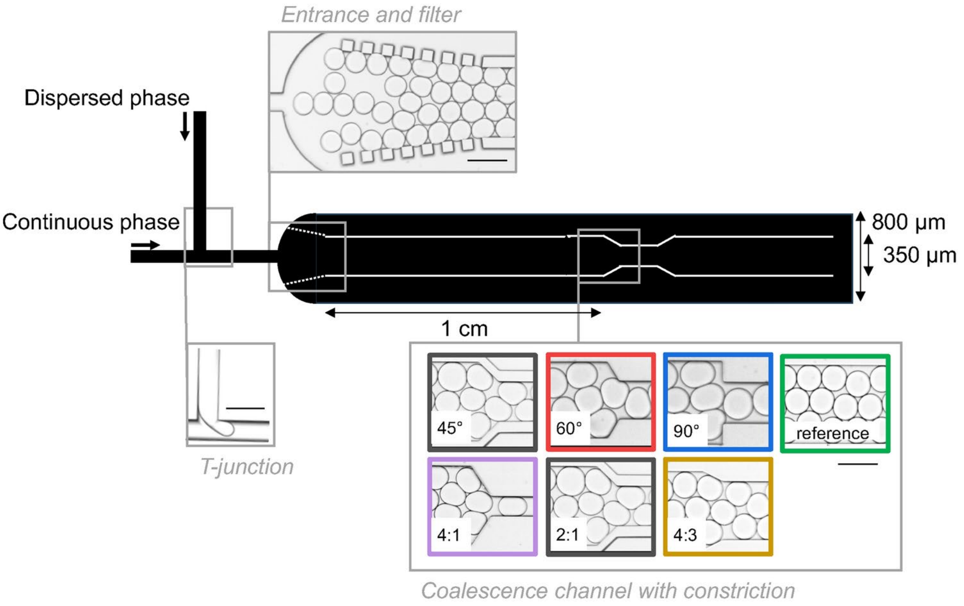

Fig. 6. Layout of the microfluidic devices. Water-in-oil droplets are continuously produced at a T-junction and packed into a concentrated emulsion using a filter consisting of seven pillars on each of the two sides (50 μm × 50 μm) that guide the droplets to the coalescence channel while enabling the passive extraction of the continuous (oil) phase through the bypass channels located aside of the coalescence channel. The bypass and coalescence channels share the same exit. Coalescence can be induced by the constriction located halfway through the 2 cm long coalescence channel. The depth of all channels was 55 μm. Scale bars: 200 μm.

LaserWriter (µmLA, Heidelberg Instruments Germany), followed by a post-bake at 100°C for 5 minutes. Developer Mr-Dev 600 (Micro Resist Technology GmbH, Germany) was used to remove the uncured photoresist and the wafer was subsequently rinsed with isopropanol, followed by a hard-bake at 200°C for 5 minutes. Before its first use, the wafer was silanized by exposing it to 1H,1H,2H,2H-perfluorooctyl-trichlorosilane vapor in a vacuum desiccator for two hours to prevent polydimethylsiloxane (PDMS) from sticking to the wafer.

The microfluidic devices were made from PDMS and prepared by mixing PDMS elastomer and curing agent (Sylgard 184 elastomer kit, Dow Corning, USA) in a 10:1 wt% ratio. PDMS was poured on the wafer, degassed in a vacuum desiccator for 30 minutes and baked at 70°C for at least two hours. PDMS was carefully peeled off and cut into separate devices. Inlets (2 mm in diameter) were punched with a revolver punch (Knipex 90 70 22), washed with isopropanol, and dried using nitrogen gas. PDMS devices were bonded to spin-coated glass slides (25 mm × 75 mm, 5:1 wt% PDMS elastomer and curing agent) using oxygen plasma exposure (Harrick, PDC-002) for 140 seconds at 0.2 - 0.4 mbar. The devices were stored at 70°C for at least 12 hours before use to allow the PDMS to recover to its hydrophobic state. No further surface modifications of the channel walls were done. The microfluidic devices were connected to the reservoirs containing the working fluids with polytetrafluoroethylene (PTFE) tubing (0.012-inch inner diameter, 1/16-inch outer diameter).

Microfluidic experiments

Demineralized water was used as the dispersed phase and hydrofluor ether (HFE-7500, $\mathrm{C_9H_5F_{15}O}$, 3M, Novec 7500, Engineering fluid) as the continuous phase with 0.05 wt% Pico-surf (Sphere Fluidics, United Kingdom). The viscosity of HFE-7500 is comparable to the viscosity of water and is equal to μ_c = 1.24 mPa s. The interfacial tension between the phases equals γ = 3.1 mN/m as measured with a pendant drop tensiometer (Krüss GmbH, Germany). The surfactant concentration was 4 times higher than the measured critical micelle concentration of Pico-surf in HFE-7500 (0.0125 wt%). In preliminary experiments, it was determined that this concentration led to stable emulsions in the reference chip (without constriction).

The liquids were supplied to the microfluidic device using a pressure controller (LU-FEZ-2000, Fluigent, Germany), and the rates of flow were measured with flow sensors (FLU-S-D and FLU-M+, Fluigent, Germany). The flows were adapted such that the dispersed phase volume fraction ranged between $75-84\%$ and the droplet diameter ranged between $100-145$ µm. The corresponding capillary number, Ca = $\mu_c v_{\mathrm{drop}}/\gamma$, with v_{drop} the velocity of droplets flowing through the main channel, ranged between 10^{-3} - 10^{-2}. The lower limit was determined by the fact that droplets jammed in the coalescence channel and newly formed droplets and continuous phase were pushed through the filter and left the device via the bypass channel. The upper limit of the Ca-range was determined by the T-junction. At higher flow rates, the system operates (first) in the jetting regime and subsequently in the parallel flow regime, resulting in a cessation of (stable) formation of droplets at the T-junction.

Microfluidic coalescence experiments

The features and the coalescence behavior of the flowing concentrated emulsions were analyzed using a high-speed camera (Phantom V9, Vision Research, USA) connected to an inverted light microscope (Axiovert S100, Carl Zeiss B.V., Germany) at a resolution of 1.87 µm/pixel. Two key features of interest are the velocity and the volume of the emulsion droplets. The features of the (non-coalesced) emulsion droplets were determined by imaging the flow upstream of the constriction at a rate of 1000 frames per second and analyzing the images using ImageJ. The obtained center of mass of each droplet in each frame was used to calculate the velocity of each droplet (v_{drop}) from the displacement of its center of mass between subsequent frames using a Matlab script (R2018B), allowing a maximum displacement of one droplet radius between the center of masses in subsequent frames and a maximum area change of 15%.

Downstream the constriction, images were recorded at 4 or 5 frames per second to determine the coalescence frequency. The two-dimensional diameter (D_{2D}) of each droplet in each frame was also determined using ImageJ. The droplet volume (V) of the pancake-like droplets was subsequently determined using[43]

$$V = \frac{\pi H}{4}\left(D_{2D}-H\right)^2 + \frac{\pi^2 H^2}{8}\left(D_{2D} - \left(1-\frac{4}{3\pi}\right)H\right),$$

with H the channel height of 55 µm. The confinement ratio, defined as the non-deformed droplet diameter ($D_{3D} = (6V/\pi)^{1/3}$) relative to the channel height (H), ranged between 1.9 and 2.4. The mean number of coalescence events (N_{coal}) was calculated from the mean of the volume of non-coalesced droplets (V_i) and the mean of the volume of all droplets (V_f) according to

$$N_{coal} = (V_f/V_i) - 1.$$

To be able to compare the coalescence behavior of concentrated emulsions for the range of studied flow rates we take the ratio between the mean number of coalescence events and the contact time as the metric for the coalescence behavior. This ratio, called the coalescence frequency (f_{coal}), is calculated as

$$f_{coal} = N_{coal}/t_{res},$$

with the residence time t_{res} calculated using the velocity of the droplets and the distance between the entrance of the coalescence channel and the constriction ($X = 1$ cm) as $t_{res} = X/v_{\mathrm{drop}}$.

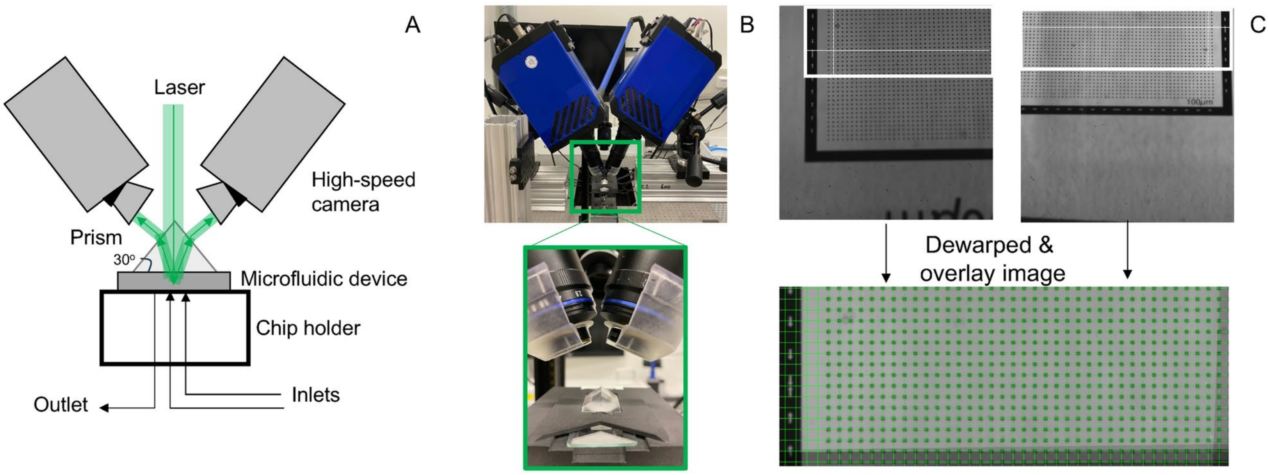

Fig. 7. (**A**) Schematic representation of the PIV set-up and the light paths. (**B**) Photographs of the PIV set-up. The caps on the lenses in the bottom image are 3D-printed holders for the long-pass filters. (**C**) Images taken with the high-speed cameras of the calibration plate at $z = 0$, which has cross-marks located every 100 µm in the $x-$ and $y-$direction. The white rectangles in the top images indicate the area that is visualized by both cameras. The bottom image is the resulting dewarped and overlay image obtained after camera calibration (1837 pixels × 56 pixels, 441 pixels per mm).

Microfluidic particle image velocimetry experiments

We designed a dedicated PIV set-up to visualize the flow profiles in the aqueous droplets of the concentrated emulsions. Rather than using the earlier used brightfield microscope, we built a PIV system with macro lenses (2.5-5x Macro lenses, focal length of 25 mm, Laowa, the Netherlands). To allow for volumetric reconstruction of the flow, we used two high-speed cameras (Imager pro HS 4M, 2016 pixels × 2016 pixels, PCO, Germany). The large focal depth of the used lenses allowed for volume reconstruction of the 55 µm high channel with only two cameras (4D-PTV) using the Shake-The-Box algorithm[41]. The cameras were tilted at angles of 35° and used in combination with a Scheimpflug adapter. The microfluidic device was placed in a 3D-printed chip holder from nylon. A prism with a height of 8 mm and 30° angles was placed on top to further decrease the Scheimpflug effect. Through this set-up, illustrated in Fig. 7A and B, we were able to record PIV images at a resolution of 441 pixels per mm and a frame rate of 1000 frames per second.

Cameras were equipped with a long pass filter (> 550 nm cut-off, FEL 0550, Thorlabs, USA). The dispersed phase was seeded with fluorescent polystyrene tracer particles with a diameter of 1.14 µm (excitation at 530 nm and emission at 607 nm, microParticles GmbH, Germany). The refractive index of the continuous fluorinated oil is 1.29[44] and of dispersed water 1.33, so no refractive index matching was performed. Particles were illuminated with a Nd:YLF laser (LDY304 PIV series, 30 mJ, 30 W, Litron Lasers, United Kingdom). Images were recorded at 1000 frames per second with a 1.28 µs exposure time. Camera calibrations were performed with images taken from a calibration plate with cross-marks located every 100 µm in the x- and y-direction (Fig. 7C). The plate was measured in the microfluidic device holder at three different z-positions with a difference of ~100 µm per step. A glass plate and the prism were placed on top of the calibration plate to mimic the optical conditions of the microfluidic experiment.

Analysis was done using DaVis 10.2.0 software (Lavision, Germany). Images obtained from the calibration plate were used for the initial calibrations using a third-order polynomial fitting, resulting in a fit error of 0.07 pixels. The experimental images were cut using a geometric mask to remove non-flow regions and used for volumetric self-calibration. Self-calibration was successfully done as the average disparity of 0.05 and 0.06 voxel were obtained for the 4:1 and 2:1 constriction channels, respectively. For PIV analysis, the initial window size was 64 voxel and then subsequently deformed to 48 and a 32 voxel interrogation windows (75% overlap). The final interrogation window size was 32 voxels (75% overlap). Tecplot 360 EX 2021 R2 was used to create the PIV figures from the mid-plane of the channel. Besides PIV, particle tracking velocimetry (PTV) was performed to obtain insights into flow structures smaller than the PIV interrogation windows. We used a Shake-The-Box algorithm[41], which allowed for temporarily resolved 3D-3C Lagrangian velocity fields. An intensity threshold of 10 counts for 2D particle detection and an allowed triangulation error of 1.4 voxels were used. After initialization, the particle positions were shaken into place by 0.1 voxels after 4 iterations of the outer and the inner loop. The maximum absolute change in particle shift was 1.0 voxel with a maximum relative change of 20%. A particle track was defined when a particle was tracked over at least four time frames.

Data availability

The datasets used and/or analyzed during the current study are available from the corresponding author upon reasonable request.

Received: 12 July 2024; Accepted: 17 January 2025

References

1. Goodarzi, F. & Zendehboudi, S. A comprehensive review on emulsions and emulsion stability in chemical and energy industries. *Can. J. Chem. Eng.* **97**, 281–309. https://doi.org/10.1002/cjce.23336 (2019).
2. Kaur, S. & Leal, L. G. Drop deformation and break-up in concentrated suspensions. *J. Rheol.* **54**, 981–1008. https://doi.org/10.1122/1.3462306 (2010).
3. Chatzigiannakis, E., Veenstra, P., ten Bosch, D. & Vermant, J. Mimicking coalescence using a pressure-controlled dynamic thin film balance. *Soft Matter* **16**, 9410–9422. https://doi.org/10.1039/D0SM00784F (2020).
4. Chesters, A. K. The modelling of coalescence processes in fluid-liquid dispersions: A review of current understanding. *Chem. Eng. Res. Des.* **69**, 259–270 (1991).
5. Kamp, J., Villwock, J. & Kraume, M. Drop coalescence in technical liquid/liquid applications: a review on experimental techniques and modeling approaches. *Rev. Chem. Eng.* **33**, 1–47. https://doi.org/10.1515/revce-2015-0071 (2017).
6. Chan, D. Y. C., Klaseboer, E. & Manica, R. Film drainage and coalescence between deformable drops and bubbles. *Soft Matter* **7**, 2235–2264. https://doi.org/10.1039/C0SM00812E (2011).
7. Bera, B., Khazal, R. & Schroën, K. Coalescence dynamics in oil-in-water emulsions at elevated temperatures. *Sci. Rep.* **11**, 10990. https://doi.org/10.1038/s41598-021-89919-5 (2021).
8. Dudek, M., Fernandes, D., Helno Herø, E. & Øye, G. Microfluidic method for determining drop-drop coalescence and contact times in flow. *Colloids Surf. A* **586**, 124265. https://doi.org/10.1016/j.colsurfa.2019.124265 (2020).
9. Krebs, T., Schroën, K. & Boom, R. Coalescence dynamics of surfactant-stabilized emulsions studied with microfluidics. *Soft Matter* **8**, 10650. https://doi.org/10.1039/c2sm26122g (2012).
10. Baret, J.-C., Kleinschmidt, F., El Harrak, A. & Griffiths, A. D. Kinetic aspects of emulsion stabilization by surfactants: a microfluidic analysis. *Langmuir* **25**, 6088–6093. https://doi.org/10.1021/la9000472 (2009).
11. Mazutis, L. & Griffiths, A. D. Selective droplet coalescence using microfluidic systems. *Lab Chip* **12**, 1800. https://doi.org/10.1039/c2lc40121e (2012).
12. Bremond, N., Thiam, A. R. & Bibette, J. Decompressing emulsion droplets favors coalescence. *Phys. Rev. Lett.* **100**, 024501. https://doi.org/10.1103/PhysRevLett.100.024501 (2008).
13. Gunes, D. Z., Clain, X., Breton, O., Mayor, G. & Burbidge, A. S. Avalanches of coalescence events and local extensional flows - Stabilisation or destabilisation due to surfactant. *J. Colloid Interface Sci.* **343**, 79–86. https://doi.org/10.1016/j.jcis.2009.11.035 (2010).
14. Leal, L. G. Flow induced coalescence of drops in a viscous fluid. *Phys. Fluids* **16**, 1833–1851. https://doi.org/10.1063/1.1701892 (2004).
15. Berry, J. D. & Dagastine, R. R. Mapping coalescence of micron-sized drops and bubbles. *J. Colloid Interface Sci.* **487**, 513–522. https://doi.org/10.1016/j.jcis.2016.10.040 (2017).
16. Bremond, N., Domejean, H. & Bibette, J. Propagation of drop coalescence in a two-dimensional emulsion: a route towards phase inversion. *Phys. Rev. Lett.* **106**, 214502. https://doi.org/10.1103/PhysRevLett.106.214502 (2011).
17. Yi, H., Fu, T., Zhu, C. & Ma, Y. Cascade coalescence of droplets in a sudden expansion microchannel. *Chem. Eng. J.* **442**, 136240. https://doi.org/10.1016/j.cej.2022.136240 (2022).
18. Zagnoni, M., Baroud, C. N. & Cooper, J. M. Electrically initiated upstream coalescence cascade of droplets in a microfluidic flow. *Phys. Rev. E* **80**, 046303. https://doi.org/10.1103/PhysRevE.80.046303 (2009).
19. Gunes, D. Z., Bercy, M., Watzke, B., Breton, O. & Burbidge, A. S. A study of extensional flow induced coalescence in microfluidic geometries with lateral channels. *Soft Matter* **9**, 7526. https://doi.org/10.1039/c3sm50751c (2013).
20. Danny Raj, M., Sivakumar, P. & Nabeel, A. Inferring the stability of concentrated emulsions from droplet configuration information. *Eur. Phys. J. Special Top.* **232**, 893–900. https://doi.org/10.1140/epjs/s11734-022-00705-4 (2022).
21. Danny Raj, M. & Rengaswamy, R. Coalescence of drops in a 2D microchannel: critical transitions to autocatalytic behaviour. *Soft Matter* **12**, 115–122. https://doi.org/10.1039/C5SM01915J (2016).
22. Lai, A., Bremond, N. & Stone, H. A. Separation-driven coalescence of droplets: an analytical criterion for the approach to contact. *J. Fluid Mech.* **632**, 97–107. https://doi.org/10.1017/S0022112009007320 (2009).
23. Cabral, J. T. & Hudson, S. D. Microfluidic approach for rapid multicomponent interfacial tensiometry. *Lab Chip* **6**, 427. https://doi.org/10.1039/b511976f (2006).
24. Brosseau, Q., Vrignon, J. & Baret, J.-C. Microfluidic dynamic interfacial tensiometry. *Soft Matter* **10**, 3066. https://doi.org/10.1039/c3sm52543k (2014).
25. Hinderink, E. B. A. et al. Early film formation in protein-stabilised emulsions: insights from a microfluidic approach. *Food Hydrocolloids* **118**, 106785. https://doi.org/10.1016/j.foodhyd.2021.106785 (2021).
26. Kovalchuk, N. M. & Simmons, M. J. Review of the role of surfactant dynamics in drop microfluidics. *Adv. Coll. Interface. Sci.* **312**, 102844. https://doi.org/10.1016/j.cis.2023.102844 (2023).
27. Gai, Y., Kim, M., Pan, M. & Tang, S. K. Y. Amphiphilic nanoparticles suppress droplet break-up in a concentrated emulsion flowing through a narrow constriction. *Biomicrofluidics* **11**, 034117. https://doi.org/10.1063/1.4985158 (2017).
28. He, L., Luo, Z. & Bai, B. Breakup of pancake droplets flowing through a microfluidic constriction. *Chem. Eng. Sci.* **220**, 115649. https://doi.org/10.1016/j.ces.2020.115649 (2020).
29. Rosenfeld, L., Fan, L., Chen, Y., Swoboda, R. & Tang, S. K. Y. Break up of droplets in a concentrated emulsion flowing through a narrow constriction. *Soft Matter* **10**, 421–430. https://doi.org/10.1039/C3SM51843D (2014).
30. Bick, A. D. & Tang, S. K. Y. Effect of volume fraction on droplet break-up in an emulsion flowing through a microfluidic constriction. *Appl. Phys. Lett.* **115**, 093702. https://doi.org/10.1063/1.5115517 (2019).
31. Chinaud, M., Voulgaropoulos, V. & Angeli, P. Surfactant effects on the coalescence of a drop in a Hele-Shaw cell. *Phys. Rev. E* **94**, 033101. https://doi.org/10.1103/PhysRevE.94.033101 (2016).
32. Jin, B.-J. & Yoo, J. Y. Visualization of droplet merging in microchannels using micro-PIV. *Exp. Fluids* **52**, 235–245. https://doi.org/10.1007/s00348-011-1221-0 (2012).
33. Kim, J. & Longmire, E. K. Investigation of binary drop rebound and coalescence in liquids using dual-field PIV technique. *Exp. Fluids* **47**, 263–278. https://doi.org/10.1007/s00348-009-0659-9 (2009).
34. Rahman, M. M., Lee, W., Iyer, A. & Williams, S. J. Viscous resistance in drop coalescence. *Phys. Fluids* **31**, 012104. https://doi.org/10.1063/1.5064706 (2019).
35. Liu, Z., Wang, X., Cao, R. & Pang, Y. Droplet coalescence at microchannel intersection chambers with different shapes. *Soft Matter* **12**, 5797–5807. https://doi.org/10.1039/C6SM01158F (2016).
36. Kovalchuk, N., Chowdhury, J., Schofield, Z., Vigolo, D. & Simmons, M. Study of drop coalescence and mixing in microchannel using Ghost Particle Velocimetry. *Chem. Eng. Res. Des.* **132**, 881–889. https://doi.org/10.1016/j.cherd.2018.01.034 (2018).
37. Leong, C. M., Gai, Y. & Tang, S. K. Y. Internal flow in droplets within a concentrated emulsion flowing in a microchannel. *Phys. Fluids* **28**, 112001. https://doi.org/10.1063/1.4968526 (2016).
38. Leong, C. M., Gai, Y. & Tang, S. K. Y. Internal flow inside droplets within a concentrated emulsion during droplet rearrangement. *Phys. Fluids* **30**, 032002. https://doi.org/10.1063/1.5020313 (2018).

39. Mohamed-Kassim, Z. & Longmire, E. K. Drop coalescence through a liquid/liquid interface. *Phys. Fluids* **16**, 2170–2181. https://doi.org/10.1063/1.1735686 (2004).
40. Ortiz-Dueñas, C., Kim, J. & Longmire, E. K. Investigation of liquid-liquid drop coalescence using tomographic PIV. *Exp. Fluids* **49**, 111–129. https://doi.org/10.1007/s00348-009-0810-7 (2010).
41. Schanz, D., Gesemann, S. & Schröder, A. Shake-The-Box: Lagrangian particle tracking at high particle image densities. *Exp. Fluids* **57**, 70. https://doi.org/10.1007/s00348-016-2157-1 (2016).
42. Williams, Y. O., Schroën, K. & Corstens, M. N. A microfluidic method to systematically study droplet stability in highly concentrated emulsions. *J. Food Eng.* **352**, 111535. https://doi.org/10.1016/j.jfoodeng.2023.111535 (2023).
43. Muijlwijk, K., Hinderink, E., Ershov, D., Berton-Carabin, C. & Schroën, K. Interfacial tension measured at high expansion rates and within milliseconds using microfluidics. *J. Colloid Interface Sci.* **470**, 71–79. https://doi.org/10.1016/j.jcis.2016.02.041 (2016).
44. Tang, S. K. Y. et al. A multi-color fast-switching microfluidic droplet dye laser. *Lab Chip* **9**, 2767. https://doi.org/10.1039/b914066b (2009).

Acknowledgements

This publication is part of a project called ‘Controlling Multiphase Flow’ and is financially supported by the Institute for Sustainable Process Technology (ISPT) and co-funded by the Dutch Research Council (NWO) and TKI-E&I with the supplementary grant ’TKI-Toeslag’ for Topconsortia for Knowledge and Innovation (TKI’s) of the Ministry of Economic Affairs and Climate Policy. More information can be found at https://ispt.eu/projects/cmf/. Authors would like to thank Prof. Dr. Christian Poelma for insightful discussions about this work.

Author contributions

C.S and E.H performed the PIV and PTV investigation, including methodology. E.H. performed the formal analysis and wrote the original draft. V.S., B.B and E.H, were responsible for conceptualization and discussed the results. All authors reviewed and edited the manuscript.

Declarations

Competing interests

The authors declare no competing interests.

Additional information

Supplementary Information The online version contains supplementary material available at https://doi.org/10.1038/s41598-025-87291-2.

Correspondence and requests for materials should be addressed to E.H.

Reprints and permissions information is available at www.nature.com/reprints.

Publisher’s note Springer Nature remains neutral with regard to jurisdictional claims in published maps and institutional affiliations.